



PAPER

[View Article Online](#)
[View Journal](#) | [View Issue](#)Cite this: *Nanoscale Adv.*, 2024, 6, 3857

Low-cost one-pot synthesis of hydrophobic and hydrophilic monodispersed iron oxide nanoparticles†

Sohel Reja, * Manoj Kumar and Sukumaran Vasudevan 

The synthesis of Superparamagnetic Iron Oxide Nanoparticles (SPIONs) with size and shape tunability, which is also industrially scalable, remains challenging. Surface functionalization of the nanoparticles is yet another active research subject. Although a variety of inorganic and organometallic precursors have been tried, which are demanding in terms of both cost and effort, the use of iron hydroxide, a simple and cheap iron precursor, has not been explored in detail for the synthesis of SPIONs following a thermal decomposition route. Here, we outline a simple one-pot thermal decomposition route that avoids separate precursor preparation and purification steps and, consequently, is easily scalable. The method involves the alcoholic hydrolysis of a simple iron salt into iron hydroxide, which, on addition of oleic acid, forms the precursor oleate complex *in situ*, which is subsequently thermally decomposed to produce monodispersed SPIONs. Minor modifications allow for particle dimensions (5–20 nm) and morphology (spheroid or cuboid) to be controlled. Additionally, we explored a simple ligand exchange process for rendering the hydrophobic nanoparticles hydrophilic. Trisodium nitrilotriacetate (NTA), a readily available polycarboxylate, can efficiently transfer the oleate-coated SPIONs to water without the need for separation from the crude reaction mixture. X-ray Rietveld refinement showed that particles obtained by this method had both the magnetite and wustite phases of iron oxide present. Magnetic measurements confirm that the iron oxide particles are superparamagnetic at room temperature, with typical blocking temperatures of 183 K for the spherical and 212 K for the cuboid ones.

Received 3rd May 2024
Accepted 12th June 2024

DOI: 10.1039/d4na00371c

rsc.li/nanoscale-advances

Introduction

Superparamagnetic iron oxide nanoparticles (SPIONs) have been extensively investigated as promising candidates for numerous applications ranging from heavy metal removal,^{1,2} wastewater treatment,^{3–5} catalysis,^{6,7} drug delivery,^{8–10} contrast agents^{11–13} and cancer treatment.^{14–16} The promise stems from the fact that their saturation magnetization is remarkably high, and secondly, being superparamagnetic, the particles do not retain any net magnetism after the magnetic field is removed.¹⁷ The latter ensures that the dispersions exhibit excellent colloidal stability.¹⁸ It is, therefore, not surprising that the synthesis of superparamagnetic iron oxide nanoparticles has been a widely explored subject.

The synthesis of iron oxide nanoparticles is a fairly complex multistep process that involves precursor preparation, formation of monomer units, nucleation and growth of the nanocrystals, and subsequent stabilization.^{19–22} The optimization of the synthetic route is of utmost importance since a small

variation in the preparative conditions can significantly impact the final outcome.^{23–26} Among the more popular methods are coprecipitation, thermal decomposition, microemulsion, and hydrothermal.^{27–29} Coprecipitation is perhaps the simplest of all: the precipitation of a 1 : 1 molar mixture of Fe(II) and Fe(III) salts in the basic medium at ambient conditions.^{30,31} The method, however, suffers from poor morphological control, problems of aggregation, and chemical instability of the produced nanoparticles. The microemulsion method tackles the above limitations by executing an intramicellar nucleation and growth process, wherein the nanoparticle size can be modulated by defining the oil/water or water/oil pool dimension.^{32,33} In the hydrothermal method, the precursor material follows a vapor phase reaction in a sealed container at a high temperature and pressure.^{34,35} Poor scalability of the last two methods is, however, a serious issue. The thermal decomposition route has often been reported as a superior method since two very crucial steps of nanoparticle formation, nucleation, and growth, are well separated by a temperature barrier, resulting in excellent particle size uniformity.^{19,36–38} The thermal decomposition route for the synthesis of iron oxide nanoparticles requires the treatment of an iron precursor in a high-boiling solvent. The precursor iron complexes are typically iron oleate, iron acetylacetonate, iron pentacarbonyl, iron(oxy)

Department of Inorganic and Physical Chemistry, IISc Bangalore, India. E-mail: sohelreja@iisc.ac.in

† Electronic supplementary information (ESI) available. See DOI: <https://doi.org/10.1039/d4na00371c>



hydroxides, *etc.* Despite the wide range of precursors to choose from, there are associated drawbacks with each. Iron(oxy) hydroxides, for example, are prepared by treating iron salts in a highly basic medium, followed by thorough washing.³⁹ These extra processing steps are demanding both in terms of time and effort. Another popular option is iron acetylacetonate. Although commercially available, it is not the primary precursor and does not participate directly in nanoparticle formation.^{40,41} Due to its much lower decomposition temperature, an early decomposition of iron acetylacetonate is observed, followed by its conversion to iron oleate, which subsequently decomposes to produce iron oxide nanoparticles. To shift the equilibrium towards the formation of iron oxide, the acetylacetonate must be removed from the reaction medium. If not completely removed, the presence of mixed ligands in the reaction medium significantly affects the particle morphology and composition.⁴² The use of organometallic precursors like iron pentacarbonyl or cupferron^{43–45} is both expensive and demanding as they must be handled under an inert atmosphere. Iron oleate, on the other hand, serves as an excellent precursor material for the scaled-up synthesis of highly monodispersed iron oxide nanoparticles.^{37,46} Iron oleate is prepared by treating iron chloride with sodium oleate in a mixed solvent system comprising water, alcohol, and a non-polar hydrocarbon. However, demanding extraction and purification steps adds to the production cost. Hydrated iron oleate, a result of incomplete drying, results in polydispersity of the thermally decomposed iron oxide nanocrystals. In the preparation of iron oxide nanocubes, the final results are heavily impacted by the degree of hydration of the precursor oleates.^{47–49} Even a trace amount of water present in the precursor oleate can form micelles with sodium oleate. As a result, oleate ions are unavailable to drive surface-specific growth, finally resulting in nanocubes with ill-defined edges.²³ The highly viscous tar-like iron oleate complex also poses a serious challenge for quantitative measurements.

Surface functionalization of the thermally decomposed nanoparticles has been a field of equal interest as the synthesis itself. Several direct and indirect functionalization strategies have been developed, including ligand exchange, capping agent oxidation, surfactant removal, polymer coating, and inorganic shell formation.⁵⁰ However, such strategies require the thermally decomposed product to be extensively processed first, which involves precipitation of nanocrystals from the crude reaction mixture followed by thorough washing for complete removal of the excess capping agent and, finally, redispersion in a suitable solvent for further functionalization. A simple and general phase-transfer protocol that can directly transfer the oleic acid-capped hydrophobic nanoparticles to an aqueous medium without the need for separation from the mother mixture is largely missing.⁵¹

A synthetic protocol that combines the simplicity of the coprecipitation method with the superior particle attributes of the thermal decomposition route would be the perfect choice. A realization of such an idea would be a one-pot synthesis that uses an inexpensive precursor with highly monodispersed nanocrystals as the final product. Since thermal decomposition is a complex multistep process, partial or complete elimination

of one or more steps will simplify the synthetic protocol significantly. This work attempts to accomplish the same by cutting down the *ex situ* precursor synthesis and processing steps. In this work, we report a rapid one-pot synthesis of both spherical and cubic iron oxide nanoparticles following a modified thermal decomposition route starting with simple Fe(III) salt. Alcoholic hydrolysis of iron salt produces iron hydroxide. The use of iron hydroxide as a metal precursor in the thermal decomposition process has remained vastly unexplored. Following the addition of oleic acid to iron hydroxide, the *in situ* preparation of the precursor oleate avoids the involved purification steps required by the traditional thermal decomposition route. In addition, a functionalization strategy has been developed using a readily available amino-polycarboxylic acid, trisodium nitrilotriacetate (NTA), which finds extensive use in the detergent industry as a chelating agent. NTA-assisted direct phase transfer of the oleate-capped hydrophobic nanoparticles avoids the need for separation and purification of the nanoparticles from the crude reaction mixture.

Experimental

Materials

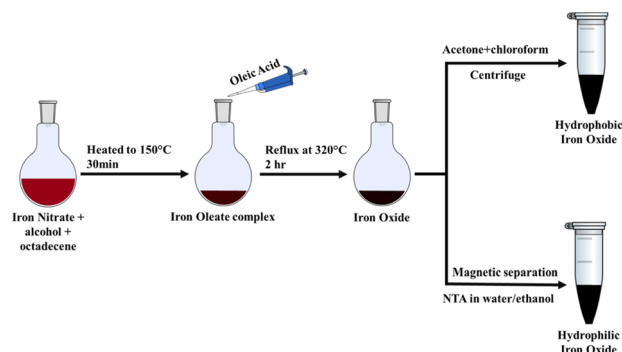
Ferric nitrate nonahydrate ($\text{Fe}(\text{NO}_3)_3 \cdot 9\text{H}_2\text{O}$), sodium oleate, methanol, ethanol, 1-propanol, isopropanol, 2-butanol, isobutanol, acetone, *n*-hexane, and chloroform were purchased from SD Fine Chemicals. Oleic acid, trisodium nitrilotriacetate monohydrate (NTA), and 1-octadecene were provided by Sigma-Aldrich. All chemicals were used as received without further purification.

Iron oxide nanoparticle synthesis

In a typical synthesis, 2 mmol $\text{Fe}(\text{NO}_3)_3 \cdot 9\text{H}_2\text{O}$ was added to 30 ml of isobutanol and 8 ml of 1-octadecene in a round-bottom flask with stirring. The red-brown solution was heated to 150 °C for 30 minutes, followed by the addition of 12 mmol of oleic acid. The solution was refluxed at 320 °C for two hours under a nitrogen blanket till the reaction was complete. The system was left to cool, and subsequently, 30 ml of a 2 : 1 mixture of acetone and chloroform was added to precipitate iron oxide. The precipitate was separated by centrifugation at 7000 rpm for 5 minutes, and the centrifugate was washed with acetone to remove oleic acid and octadecene and was then dried in an oven at 60 °C. The obtained product was readily dispersible in nonpolar solvents such as chloroform, hexane, and toluene. As described in the following section, the procedure gave a subsequent iron oxide nanoparticle. Subsequent experiments were repeated with other simple alcohols (methanol, ethanol, isopropanol, 1-propanol) instead of isobutanol as the solvent for iron nitrate.

Iron oxide nanoparticles were also prepared by modifying the procedure outlined in Scheme 1 by replacing oleic acid with a mixture of surfactants: (a) 8 mmol of oleyl alcohol along with 8 mmol of oleic acid and (b) 2 mmol Na-oleate and 8 mmol oleic acid, with the rest of the procedure remaining unchanged. It





Scheme 1 Schematic of the preparative procedure.

was found that the modified procedure gave iron oxide nanoparticles with different particle dimensions and morphology.

Phase transfer of nanoparticles. A solution containing 20 mmol NTA in 30 ml hot water ($\sim 60^\circ\text{C}$) was added to oleic acid-capped iron oxide nanoparticles in octadecene (as described in the previous section) at room temperature, followed by 60 ml of ethanol. After the addition of 30 ml toluene, the dispersion was stirred vigorously for 2 hours at 80°C under a refluxing condition. The iron oxide nanoparticles transferred from the oil to the aqueous phase, followed by their magnetic separation and subsequent washing with ethanol and acetone. The as-produced nanoparticles were readily dispersible in water.

Characterization

The phase composition of the nanocrystals was determined by a PANalytical Empyrean X-ray diffractometer equipped with a Pixel 3D detector with $\text{Cu-K}\alpha$ radiation. The size and shape evolution of the nanocrystals were studied with a JEOL JEM 2100F transmission electron microscope. Magnetic properties were measured with Quantum Designs PPMS 9T 639. Bruker ALPHA-II Compact ATR-FTIR was used to record infrared spectroscopy. Malvern Zetasizer ZS has been used for zeta potential analysis.

Results and discussion

Synthesis of iron oxide nanoparticles

Iron oxide nanoparticles were synthesized following the procedure outlined in the experimental section. The reaction is fairly straightforward. Alcoholic solutions of iron nitrate have been studied extensively in relation to spray flame pyrolysis.^{52,53} Assuming the complete dissolution of the iron nitrate in alcohol and the ionic dissociation of the water of hydration, the following equilibrium occurs in the solution



If the solution is left undisturbed, the solution turns turbid, and the iron hydroxide precipitates out of the reaction medium, as confirmed by IR and XRD (ESI, Fig. S1†). The alcoholic

hydrolyzed solution containing iron hydroxide, when heated, decomposition of nitrate is observed, as inferred by the appearance of brown fume. With the further addition of oleic acid, iron hydroxide forms an iron oleate complex (ESI, Fig. S2†). At an elevated temperature, the iron oleate complex decomposes to produce iron oxide nanoparticles. The scalability of the current protocol was tested with 30 mmol of iron nitrate, and a yield of 94% was noted. The as-produced iron oxide nanoparticles were highly monodispersed (ESI, Fig. S10†).

The PXRD pattern of the products of Scheme 1 is shown in Fig. 1a. The alcohol used in the preparation was isobutanol. Rietveld analysis of the diffraction pattern produced the best fit with a phase combination of 98.9% magnetite (Fe_3O_4 ; ref no: 96-900-5840) and 1.1% wustite (FeO ; ref no: 96-900-9768), rather than a single component (magnetite or wustite).

The TEM image of the iron oxide nanoparticles prepared by Scheme 1 using isobutanol as the starting alcohol is shown in Fig. 1b. The image shows monodispersed nanoparticles with an average particle size of 11 nm. The dimensions are in good agreement with the size estimate obtained from the PXRD data (10 nm) using the Debye–Scherrer equation. The selected area electron diffraction (SAED) exhibits discrete bright dots that could be indexed to the (220), (311), (400), (511), and (440) planes of the pure spinel iron oxide phase (ESI, Fig. S3a†). The TEM images show the presence of particles exhibiting different contrast. An HRTEM image of the light and dark particles (Fig. 1c and d) showed fringes that correspond to different planes of either the magnetite (Fe_3O_4) or wustite (FeO) structures. Particles with darker contrast (Fig. 1c) have their [0,0,1] zone axis parallel to the beam. For these particles, the HRTEM

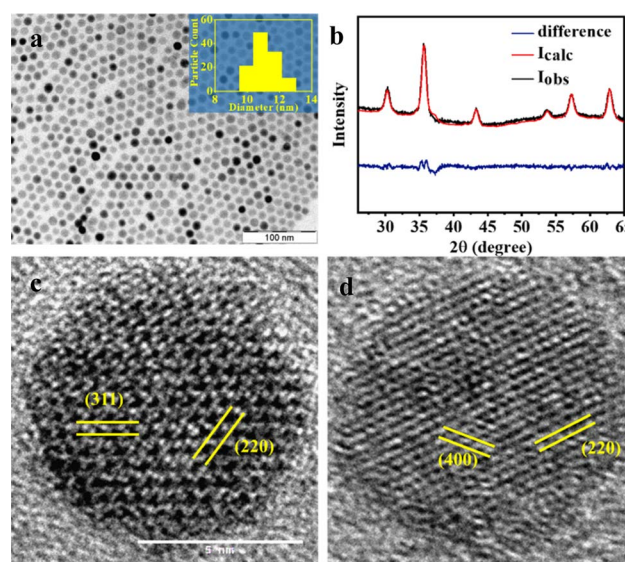


Fig. 1 (a) TEM image of the nanoparticles and the corresponding particle size histogram in the inset; (b) PXRD pattern of the products of Scheme 1. The red line is best fit from a Rietveld analysis using a mixture of phases, magnetite, and wustite. The difference between the experiment and the Rietveld fit is shown in blue: indexed HRTEM image of the particles with (c) darker and (d) lighter contrast matches well with the magnetite phase.



shows lattice fringes with the characteristic spacings of the (2,2,0) and (4,0,0) planes of magnetite, as confirmed from the diffraction pattern generated from the lattice image by a Fast Fourier Transform (FFT) (ESI, Fig. S3c†). Particles with lighter contrast (Fig. 1d) have their [1, -1, -2] zone axis parallel to the beam. The FFT of these particles shows diffraction spots corresponding to the (3,1,1) and (2,2,0) planes of magnetite (ESI, Fig. S3d†).³⁹

As mentioned earlier, the synthesis of iron oxide nanoparticles could also be realized if isobutanol, used for dissolving the iron nitrate in Scheme 1a, is replaced by other alcohols – methanol, ethanol, isopropanol, and 1-propanol. In all cases, the PXRD patterns were similar. The TEM images showed that the particle morphologies and dimensions, too, were similar (ESI Table S2†), irrespective of the alcohol used (ESI Fig. S7†). The results are not surprising since once iron nitrate hydrolyses, producing iron hydroxide, the solvent alcohol has little role to play in the subsequent steps. Control of particle size may, however, be obtained by varying the reflux time. The particle sizes could be varied from 8 nm to 20 nm (ESI, Table S1†) when the reflux time was changed from 30 minutes to 6 hours (Fig. 2). Formation of larger nanoparticles with longer reflux time is a direct consequence of the prolonged growth phase, which is in accordance with Ostwald's ripening mechanism.⁵⁴

The addition of oleyl alcohol along with oleic acid has a profound influence on the particle size. Oleyl alcohol acts as a mild reducing agent, lowering the decomposition temperature of the iron oleate complex, leading to smaller particles.^{55,56} The TEM images show a fairly monodispersed distribution with a mean particle size of 5 nm (Fig. 3a). A Rietveld analysis of the PXRD data gave the best fit for a mixture of 99% magnetite and 1% wustite (Fig. 3b). The lattice planes in the HRTEM (Fig. 3c and d), indexed by evaluating *d*-spacing from the FFT-generated diffraction pattern, were found to match with (220) and (311) planes of the spinel phase of iron oxide (ESI, Fig. S4†).

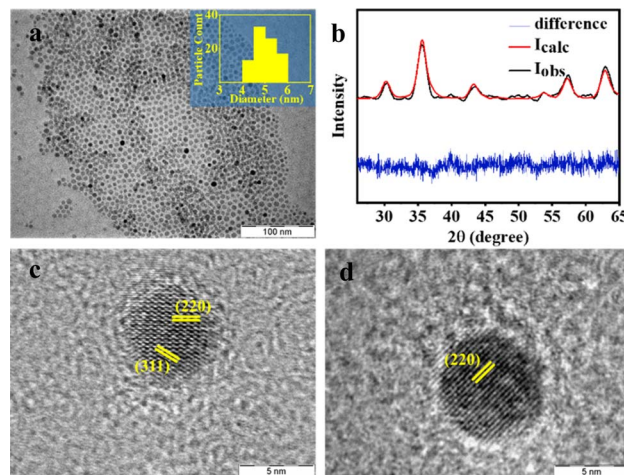


Fig. 3 (a) TEM image of particles prepared by Scheme 1 using a 1 : 1 mixture of oleyl alcohol and oleic acid. The inset shows a histogram of particle sizes; (b) the corresponding PXRD pattern, along with Rietveld refinement. The difference between the experiment and the fit is shown in blue. HRTEM image of a particle with lighter (c) and darker (d) contrast with the indexed lattice planes.

While the addition of oleyl alcohol promoted the formation of smaller particles, morphology can be controlled by the addition of sodium oleate along with oleic acid. Employing a mixture of oleic acid and sodium oleate resulted in the formation of nanocubes of the average side of 13 nm (Fig. 4a). A Rietveld analysis of the PXRD patterns (Fig. 4b) indicated a mixture of 92.6% magnetite and 7.4% wustite. An HRTEM analysis showed, however, that both the light and darker particles exhibited an identical fringe corresponding to the

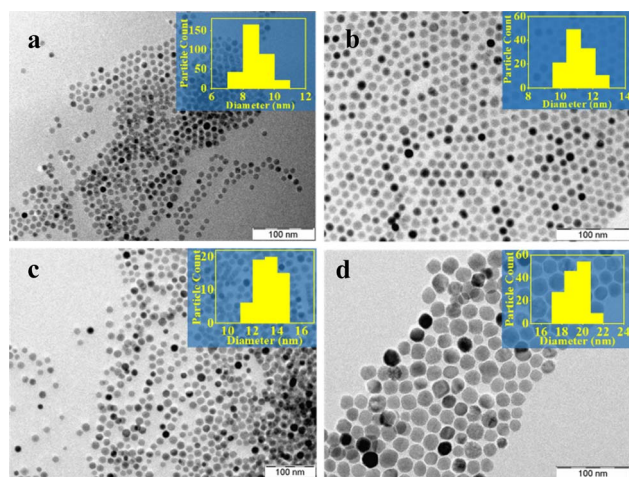


Fig. 2 TEM images of iron oxide particles prepared by Scheme 1 for different reflux times (a) 0.5 hours, (b) 2 hours, (c) 4 hours, and (d) 6 hours (inset shows particle size histogram).

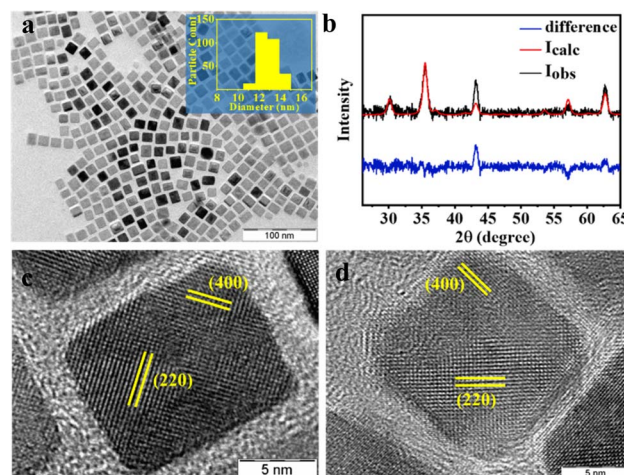


Fig. 4 (a) TEM images of iron oxide particles obtained when a mixture of oleic acid and sodium oleate is used in Scheme 1. The inset shows the particle size histogram and (b) the corresponding PXRD pattern. The red line is the best fit from a Rietveld analysis. The difference between the experiment and the Rietveld fit is shown in blue. HRTEM images of particles with (c) darker and (d) lighter contrast. The indexed lattice fringes correspond to the (220) and (400) diffraction planes of the iron oxide spinel phase.



(220) and (400) diffraction plane of the iron oxide spinel phase (Fig. 4c and d). SAED and indexed FFT confirm the same (ESI, Fig. S5a, c and d†). The difference, in contrast, is therefore not due to differences in the zone axis of the particles in the TEM but may be due to differences in the thickness of the particles.³⁹ The formation of particles with cuboid geometry is because sodium oleate dissociates to a much greater extent than oleic acid, leading to a high concentration of oleate ions in the reaction medium during the growth phase. Preferential adhesion of the oleate ions on {100} facets hinders the growth of that facet, resulting in nanocrystals confined by {100} planes.⁵⁷

The as-prepared iron oxide nanoparticles are dispersible in most common non-polar solvents; the presence of surface-anchored oleate ions ensures that the particles are hydrophobic. The nanoparticles can, however, be rendered hydrophilic by modifying the last step of the preparative scheme (Scheme 1). If, instead of precipitating the oleic acid-capped iron oxide nanoparticle from the octadecene media by the addition of acetone:chloroform mixture, a solution of NTA is added, the iron oxide nanoparticles are phase-transferred to the aqueous phase. The iron oxide nanoparticles obtained are readily dispersible in water (Fig. 5 inset). Usually, a zeta potential value in the range of ± 30 mV ensures a stable dispersion. The excellent water-dispersibility of the NTA-coated iron oxide nanoparticles can be well understood by considering the corresponding zeta potential value of -28 mV. The negative zeta potential indicates the presence of a carboxylate functional group on the particle surface. The aqueous dispersions of the NTA-capped iron oxide nanoparticles are stable. Visual inspection shows no evidence of particles settling down even after 3 months. Zeta-potential and dynamic light scattering (DLS) measurements of the aqueous dispersion at pH ~ 7 showed no significant change even after a gap of a week (ESI, Fig. S9†).

Infrared spectra indicate that the surface of the nanoparticles is functionalized by carboxylate groups (ESI Fig. S8a†),

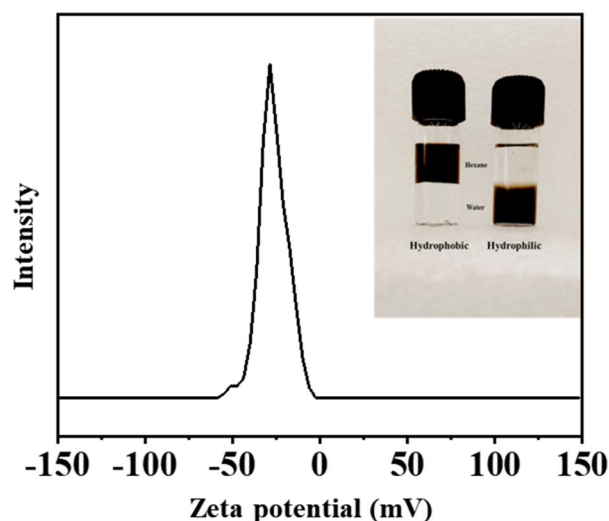


Fig. 5 Zeta potential of NTA-coated water dispersible iron oxide nanoparticles. The inset shows the photograph of phase-stabilized oleic acid-coated hydrophobic and NTA-coated hydrophilic iron oxide nanoparticles in a mixed solvent medium.

which would explain the hydrophilic nature of the particles. PXRD data confirms the presence of the spinel phase of the iron oxide phase (ESI Fig. S8b†), while the TEM images (Fig. 6) indicate that the particles retain their morphology even after phase transfer and functionalization. The indexed FFT confirms the diffraction planes corresponding to the iron oxide spinel phase (ESI Fig. S6†). The particles exhibit a much greater degree of aggregation as compared to the oleate-capped particles (Fig. 1b). This is not surprising as the surface carboxylates, apart from being much shorter than the oleate chains, may interact with each other *via* H-bonding.⁵⁸

The magnetic behavior of the iron oxide nanoparticles prepared in this study is similar to that reported for iron oxide nanoparticles of similar dimensions.³⁹ The temperature dependence of the magnetic moment, $M(T)$, under an applied magnetic field ($H = 0.01$ T) of the spherical and cubic nanoparticles was measured from 300 to 10 K after field cooling (FC) and after zero-field cooling (ZFC) (Fig. 7a and b). The magnetic behavior is characteristic of superparamagnetic nanoparticles exhibiting a well-defined blocking temperature, T_b , the temperature at which superparamagnetism sets in. Below T_b , the FC and ZFC magnetization curves are split, whereas, above T_b , they coincide as the remanence and coercivity have vanished. For spherical particles, the blocking temperature T_b is 183 K, but for the cubic nanocrystals, the value is higher, at 212 K. For both spherical and cubic nanoparticles, the above T_b is superparamagnetic. This was confirmed by fitting the magnetization at 300 K ($T > T_b$) as a function of the field to a modified Langevin function (Fig. 8a and b). The fits confirm the superparamagnetic nature of both the spherical and cuboid iron oxide nanoparticles at 300 K.

$$M = M_0 L(x) + \chi H$$

where $L(x) = [\coth(x) - (1/x)]$ is the Langevin function, M_0 is the saturation magnetization, and $x = \mu_p H / k_B T$, where μ_p is the

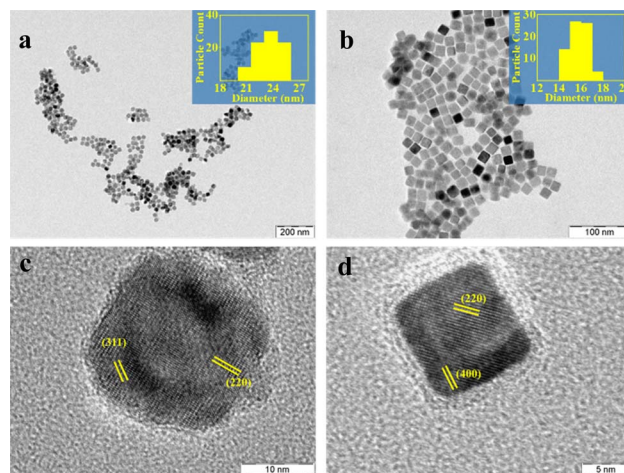


Fig. 6 TEM images of (a) phase-transferred nano spheroids and (b) nanocubes. Corresponding HRTEM images of (c) nanospheroids and (d) nanocubes show indexed lattice planes corresponding to the iron oxide spinel phase.

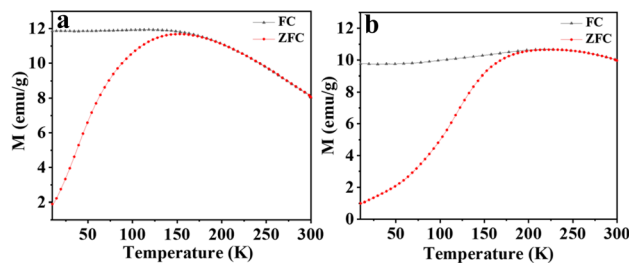


Fig. 7 ZFC-FC plot of (a) iron oxide nanospheres and (b) nanocubes.

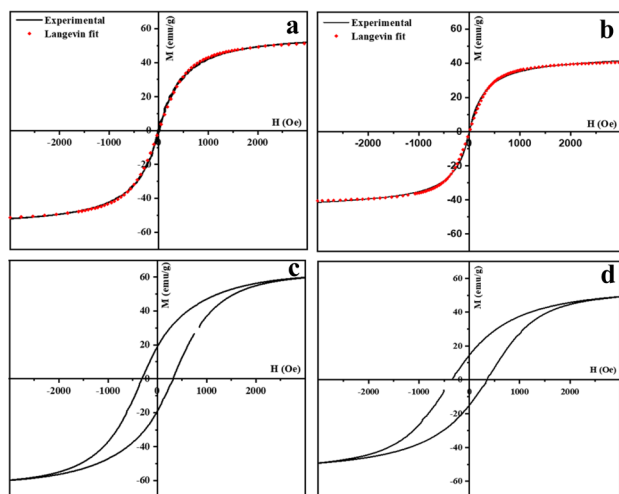


Fig. 8 Isothermal (300 K) magnetization curves for iron oxide nanocrystals (in bold lines) and corresponding modified Langevin fitting (red squares) of (a) spherical ($T_b = 183$ K) and (b) cubic ($T_b = 212$ K) morphologies above their blocking temperatures. The corresponding $M-H$ plots for iron oxide (c) nanospheres and (d) nanocubes at 10 K.

particle magnetic moment, k_B the Boltzmann constant, and x the susceptibility of the ferrimagnetic nanoparticles as predicted by Néel for particles with antiferromagnetic interactions.

The $M-H$ hysteresis loops for the iron oxide nanospheres and nanocubes recorded at 10 K are shown in Fig. 8c and d. The saturation magnetization value for the iron oxide nanospheres is 58 emu g^{-1} of nanoparticles while that of the nanocubes was 46 emu g^{-1} of nanoparticles. The difference in the blocking temperature, as well as the saturation magnetization for the spherical and cubic nanocrystals, could be a consequence of the presence of a significant proportion of antiferromagnetic wustite phase in case of nanocubes.³⁹

Conclusions

Superparamagnetic Iron Oxide Nanoparticles (SPIONs) have found extensive applications in diverse fields that include biomedicine, water remediation, and drug delivery. These applications require the development of synthetic protocols and methods that can produce SPIONs with precisely controlled size and shape, with the added caveat of being scalable. In this work,

we outline a one-pot thermal decomposition route that avoids the separate preparation and purification of precursor complexes and, consequently, is easily scalable. The method involves the alcoholic hydrolysis of iron nitrate into iron hydroxide, which, on oleic acid addition, forms iron oleate. The *in situ* formed precursor complex is then thermally decomposed to produce SPIONs that have a narrow size distribution, as confirmed by TEM images. Minor modifications, changing the reaction temperature, or addition of oleyl alcohol or sodium oleate along with oleic acid allow for particle dimensions (5–20 nm) and morphology, spheroid/cuboid, to be controlled. Additionally, the particles are readily transferred from the crude reaction media to an aqueous phase using NTA as a phase transfer agent. X-ray Rietveld Refinement showed that particles obtained by this method had both the magnetite and wustite phases of iron oxide present. The iron oxide particles are superparamagnetic at room temperature with typical blocking temperatures of 183 K for the particles with spherical morphology and 212 K for those with cuboid morphology. The significance of the present one-pot preparative method is its simplicity and, as we shall show in subsequent studies, versatility. It may be extended to the preparation of mixed metal ferrite nanoparticles while still retaining the ease of the original method.

Conflicts of interest

There are no conflicts to declare.

Acknowledgements

The authors acknowledge support from the Chemical Science Division facility, IISc, for TEM, PXRD, and IR analysis. The authors thank CeNSE and IISc for magnetism measurements.

Notes and references

- 1 V. Sharma, H. Singh, S. Guleria, N. Bhardwaj, S. Puri, S. K. Arya and M. Khatri, *Environ. Nanotechnol. Monit. Manag.*, 2022, **18**, 100716.
- 2 A. K. Inamdar, R. S. Rajenimbalkar, N. R. Hulsure, A. S. Kadam, B. H. Shinde, S. P. Patole, S. B. Shelke and S. N. Inamdar, *Mater. Today Proc.*, 2023, DOI: [10.1016/j.matpr.2023.05.527](https://doi.org/10.1016/j.matpr.2023.05.527).
- 3 V. C. Tai, H. X. Che, X. Y. Kong, K. C. Ho and W. M. Ng, *J. Ind. Eng. Chem.*, 2023, **127**, 82–100.
- 4 W. Sun, S. Wang, Z. Yu and X. Cao, *Environ. Sci. Water Res. Technol.*, 2023, **9**, 1266–1289.
- 5 M. Perwez, H. Fatima, M. Arshad, V. K. Meena and B. Ahmad, *Int. J. Environ. Sci. Technol.*, 2023, **20**, 5697–5714.
- 6 P. Kumar, V. Tomar, D. Kumar, R. K. Joshi and M. Nemiwal, *Tetrahedron*, 2022, **106–107**, 132641.
- 7 J. Sharma, P. Kumar, M. Sillanpaa, D. Kumar and M. Nemiwal, *Inorg. Chem. Commun.*, 2022, **145**, 110055.
- 8 V. Sachdeva, A. Monga, R. Vashisht, D. Singh, A. Singh and N. Bedi, *J. Drug Deliv. Sci. Technol.*, 2022, **74**, 103585.



- 9 A. Parmanik and A. Bose, *J. Drug Deliv. Sci. Technol.*, 2023, **90**, 105120.
- 10 R. Qiao, C. Fu, H. Forgham, I. Javed, X. Huang, J. Zhu, A. K. Whittaker and T. P. Davis, *Adv. Drug Deliv. Rev.*, 2023, **197**, 114822.
- 11 M. Jeon, M. V. Halbert, Z. R. Stephen and M. Zhang, *Adv. Mater.*, 2021, **33**, 1–18.
- 12 C. Chen, J. Ge, Y. Gao, L. Chen, J. Cui, J. Zeng and M. Gao, *Wiley Interdiscip. Rev. Nanomed. Nanobiotechnol.*, 2022, **14**, 1–22.
- 13 Z. Li, R. Bai, J. Yi, H. Zhou, J. Xian and C. Chen, *Chem. Biomed. Imaging*, 2023, **1**, 315–339.
- 14 Y. Zhang, X. Li, Y. Zhang, J. Wei, W. Wang, C. Dong, Y. Xue, M. Liu and R. Pei, *New J. Chem.*, 2021, **45**, 7918–7941.
- 15 L. Sun, H. Liu, Y. Ye, Y. Lei, R. Islam, S. Tan, R. Tong, Y. B. Miao and L. Cai, *Signal Transduct. Target. Ther.*, 2023, **8**, 418.
- 16 S. Chung, R. A. Revia and M. Zhang, *Nanoscale Horiz.*, 2021, **6**, 696–717.
- 17 Wahajuddin and S. Arora, *Int. J. Nanomed.*, 2012, **7**, 3445–3471.
- 18 P. O. Champagne, H. Westwick, A. Bouthillier and M. Sawan, *Nanomedicine*, 2018, **13**, 1385–1400.
- 19 G. K. Soon, Y. Piao, J. Park, S. Angappane, Y. Jo, N. M. Hwang, J. G. Park and T. Hyeon, *J. Am. Chem. Soc.*, 2007, **129**, 12571–12584.
- 20 N. T. K. Thanh, N. Maclean and S. Mahiddine, *Chem. Rev.*, 2014, **114**, 7610–7630.
- 21 J. Van Embden, A. S. R. Chesman and J. J. Jasieniak, *Chem. Mater.*, 2015, **27**, 2246–2285.
- 22 L. Wu, A. Mendoza-Garcia, Q. Li and S. Sun, *Chem. Rev.*, 2016, **116**, 10473–10512.
- 23 G. Cotin, C. Kiefer, F. Pertion, D. Ihiwakrim, C. Blanco-Andujar, S. Moldovan, C. Lefevre, O. Ersen, B. Pichon, D. Mertz and S. Bégin-Colin, *Nanomaterials*, 2018, **8**, 881.
- 24 A. Feld, A. Weimer, A. Kornowski, N. Winckelmans, J. P. Merkl, H. Kloust, R. Zierold, C. Schmidtke, T. Schotten, M. Riedner, S. Bals and H. Weller, *ACS Nano*, 2019, **13**, 152–162.
- 25 V. Fokina, M. Wilke, M. Dulle, S. Ehlert and S. Förster, *J. Phys. Chem. C*, 2022, **126**, 21356–21367.
- 26 A. Avasthi, C. Caro, M. L. Garcia-Martin and M. Pernia Leal, *React. Chem. Eng.*, 2023, **8**, 1638.
- 27 P. R. S. Baabu, H. K. Kumar, M. B. Gumpu, J. Babu K, A. J. Kulandaisamy and J. B. B. Rayappan, *Materials*, 2023, **16**.
- 28 T. Girardet, P. Venturini, H. Martinez, J. C. Dupin, F. Cleymand and S. Fleutot, *Appl. Sci.*, 2022, **12**, 8127.
- 29 P. Farinha, J. M. P. Coelho, C. P. Reis and M. M. Gaspar, *Nanomaterials*, 2021, **11**, 3432.
- 30 W. M. Daoush, *J. Nanomed. Res.*, 2017, **5**, 12–16.
- 31 H. Mohammadi, E. Nekobahr, J. Akhtari, M. Saeedi, J. Akbari and F. Fathi, *Toxicol. Rep.*, 2021, **8**, 331–336.
- 32 J. R. Vargas-Ortiz, C. Gonzalez and K. Esquivel, *Processes*, 2022, **10**, 2282.
- 33 M. Salvador, G. Gutiérrez, S. Noriega, A. Moyano, M. C. Blanco-López and M. Matos, *Int. J. Mol. Sci.*, 2021, **22**, 1–17.
- 34 N. Torres-Gómez, O. Nava, L. Argueta-Figueroa, R. García-Contreras, A. Baeza-Barrera and A. R. Vilchis-Nestor, *J. Nanomater.*, 2019, **2019**, 7921273.
- 35 D. Ramimoghadam, S. Bagheri and S. B. A. Hamid, *J. Magn. Magn. Mater.*, 2014, **368**, 207–229.
- 36 J. Park, J. Joo, G. K. Soon, Y. Jang and T. Hyeon, *Angew. Chem., Int. Ed.*, 2007, **46**, 4630–4660.
- 37 J. Park, K. An, Y. Hwang, J. E. G. Park, H. J. Noh, J. Y. Kim, J. H. Park, N. M. Hwang and T. Hyeon, *Nat. Mater.*, 2004, **3**, 891–895.
- 38 B. H. Kim, W. Ko, J. H. Kim, J. S. Georgiou, M. S. Bootharaju, J. Park and T. Hyeon, *Isr. J. Chem.*, 2023, **202200103**, 1–17.
- 39 R. Chalasani and S. Vasudevan, *J. Phys. Chem. C*, 2011, **115**, 18088–18093.
- 40 S. Sun, H. Zeng, D. B. Robinson, S. Raoux, P. M. Rice, S. X. Wang and G. Li, *J. Am. Chem. Soc.*, 2004, **126**, 273–279.
- 41 J. Xie, S. Peng, N. Brower, N. Pourmand, S. X. Wang and S. Sun, *Pure Appl. Chem.*, 2006, **78**, 1003–1014.
- 42 M. Nahorniak, P. Pasetto, J. M. Greneche, V. Samaryk, S. Auguste, A. Rousseau, N. Nosova and S. Varvarenko, *Beilstein J. Nanotechnol.*, 2023, **14**, 11–22.
- 43 J. Cheon, N. J. Kang, S. M. Lee, J. H. Lee, J. H. Yoon and S. J. Oh, *J. Am. Chem. Soc.*, 2004, **126**, 1950–1951.
- 44 B. Geng, X. Liu, J. Ma and Q. Du, *Mater. Sci. Eng. B*, 2007, **145**, 17–22.
- 45 G. M. Bhalerao, A. K. Sinha, H. Srivastava and A. K. Srivastava, *Appl. Phys. A: Mater. Sci. Process.*, 2009, **95**, 373–380.
- 46 J. Park, E. Lee, N.-M. Hwang, M. Kang, S. C. Kim, Y. Hwang, J.-G. Park, H.-J. Noh, J.-Y. Kim, J.-H. Park and T. Hyeon, *Angew. Chem.*, 2005, **117**, 2932–2937.
- 47 G. Cotin, C. Kiefer, F. Pertion, M. Boero, B. Özdamar, A. Bouzid, G. Ori, C. Massobrio, D. Begin, B. Pichon, D. Mertz and S. Bégin-Colin, *ACS Appl. Nano Mater.*, 2018, **1**, 4306–4316.
- 48 D. K. Kim and J. W. Lee, *J. Korean Ceram. Soc.*, 2018, **55**, 625–634.
- 49 M. M. Lin and D. K. Kim, *J. Nanoparticle Res.*, 2012, **14**, 688.
- 50 B. He, L. Zhou and J. Huang, *Mater. Lett.*, 2014, **117**, 142–145.
- 51 P. Guardia, A. Riedinger, S. Nitti, G. Pugliese, S. Marras, A. Genovese, M. E. Materia, C. Lefevre, L. Manna and T. Pellegrino, *J. Mater. Chem. B*, 2014, **2**, 4426–4434.
- 52 A. Keller, I. Wlokas, M. Kohns and H. Hasse, *Fluid Phase Equilib.*, 2021, **536**, 112987.
- 53 M. F. B. Stodt, M. Gonchikzhapov, T. Kasper, U. Fritsching and J. Kiefer, *Phys. Chem. Chem. Phys.*, 2019, **21**, 24793–24801.
- 54 L. T. Lu, N. T. Dung, L. D. Tung, C. T. Thanh, O. K. Quy, N. V. Chuc, S. Maenosono and N. T. K. Thanh, *Nanoscale*, 2015, **7**, 19596–19610.
- 55 B. H. Kim, N. Lee, H. Kim, K. An, Y. Il Park, Y. Choi, K. Shin, Y. Lee, S. G. Kwon, H. Bin Na, J. G. Park, T. Y. Ahn, Y. W. Kim,



- W. K. Moon, S. H. Choi and T. Hyeon, *J. Am. Chem. Soc.*, 2011, **133**, 12624–12631.
- 56 H. Zhang, L. Li, X. L. Liu, J. Jiao, C. T. Ng, J. B. Yi, Y. E. Luo, B. H. Bay, L. Y. Zhao, M. L. Peng, N. Gu and H. M. Fan, *ACS Nano*, 2017, **11**, 3614–3631.
- 57 M. V. Kovalenko, M. I. Bodnarchuk, R. T. Lechner, G. Hesser, F. Schäffler and W. Heiss, *J. Am. Chem. Soc.*, 2007, **129**, 6352–6353.
- 58 K. Woo and J. Hong, *INTERMAG ASIA 2005 Dig. IEEE Int. Magn. Conf.*, 2005, vol. 41, p. 400.

